Research Article Vol. 14, No. 6 / June 2026 / Photonics Research 2591

Single-objective two-photon oblique light sheet microscopy with a low repetition rate for 3D high-SNR imaging

Jeonggeun Song,[1] Woojin Lee,[1] Hyeong Soo Nam,[1] Hamin Park,[2] Young-Gyun Park,[2] and Hongki Yoo[1,*]

[1]Department of Mechanical Engineering, Korea Advanced Institute of Science and Technology, Daejeon 34141, Republic of Korea
[2]Department of Bio and Brain Engineering, Korea Advanced Institute of Science and Technology, Daejeon 34141, Republic of Korea
*Corresponding author: h.yoo@kaist.ac.kr

Received 16 December 2025; revised 1 April 2026; accepted 9 April 2026; posted 9 April 2026 (Doc. ID 584858); published 26 May 2026

Two-photon light sheet microscopy is a powerful technology for rapid three-dimensional (3D) fluorescence imaging with low phototoxicity, which has led to its wide adoption in biomedical and life science applications. However, conventional multiobjective lens configurations limit compatibility with large or irregularly shaped biological samples, restricting broader applicability. Moreover, image quality is often compromised due to the inherent trade-off between the low numerical aperture required for selective planar illumination and the reduced efficiency of two-photon excitation. In this study, we present a single-objective two-photon oblique light sheet microscopy (TP-ob-LSM) system employing a low-repetition-rate light source. This single-objective lens design enables simultaneous excitation and detection, thereby significantly enhancing compatibility with diverse biological sample geometries. Furthermore, by adjusting the repetition rate while maintaining constant average power, we increased pulse energy and achieved a 22.9-fold improvement in signal-to-noise ratio compared to conventional high-repetition-rate systems through system-level optimization of the excitation regime. We demonstrate large-volume reconstructions (9 mm × 6 mm × 0.18 mm) and deep-tissue imaging in 1-mm-thick mouse brain slices with clear dendritic morphology. The proposed TP-ob-LSM with low-repetition-rate excitation offers a promising solution for high-quality 3D imaging across a wide range of biomedical applications.

https://doi.org/10.1364/PRJ.584858

1. INTRODUCTION

Recent advances in biomedical imaging technologies have greatly expanded our ability to visualize biological structures and dynamic processes that were previously inaccessible. Among various imaging modalities, three-dimensional (3D) fluorescence imaging has attracted considerable attention for its ability to provide comprehensive biological information. Representative techniques include confocal microscopy [1] and nonlinear microscopy [2–7], both of which offer optical sectioning. While effective for volumetric imaging, these methods are limited by slow acquisition speed and susceptibility to photobleaching and phototoxicity.

Light sheet microscopy (LSM) has emerged as a powerful technique for rapid 3D fluorescence imaging through spatially selective planar illumination. By illuminating a thin plane and detecting fluorescence with a two-dimensional (2D) sensor, LSM achieves fast volumetric imaging without point scanning and substantially reduces photobleaching and phototoxicity [8–11]. Because of these advantages, LSM has been widely used in various biological samples such as fly embryos [12], zebrafish embryos [13,14], brain tissue [15], and mouse cardiac tissue [16].

Conventional LSM systems, however, typically employ orthogonal excitation and detection paths with separate objectives, restricting their use to small organisms or excised tissue samples [17]. To overcome these inherent limitations, single-objective LSM systems have been developed, enabling simultaneous excitation and detection through a single-objective lens. Examples include microfluidic channel-based single-objective LSM [18], axially swept plane optical microscopy [19–21], and oblique plane microscopy [22]. While these approaches simplify the optical setup, they often require complex sample preparation or suffer from vibration artifacts caused by mechanical stage translation. To address these issues, single-photon LSM systems such as SCAPE and SCAPE 2.0 employ galvanometric or polygon mirrors to scan the light sheet without mechanical translation [23,24].

Two-photon excitation (TPE) further enhances fluorescence imaging by employing near-infrared excitation

wavelengths, which experience reduced scattering and absorption in biological tissues and therefore enable deeper tissue imaging [25–27]. Compared with single-photon excitation, which offers simpler optical implementation and lower system cost, TPE provides several important advantages for imaging thick and highly scattering biological tissues. Because two-photon fluorescence is generated only in regions of sufficiently high photon density, TPE inherently suppresses out-of-focus background signals, improves image contrast, and reduces photodamage outside the focal region. These advantages have made two-photon microscopy (TPM) a widely adopted tool in biomedical research. TPM is utilized for imaging both exogenous fluorescent probes and endogenous fluorophores such as collagen, elastin [28,29], NADH, and FAD [30]. It has also been applied in the diagnosis and study of brain tissue [31], atherosclerotic plaques [32,33], and liver fibrosis [34]. Recently, two-photon light sheet microscopy (TP-LSM) has attracted growing interest by combining the benefits of TPE and LSM to rapidly acquire high-quality 3D fluorescence images from thick biological samples [35–37].

Despite its advantages, TP-LSM still faces inherent trade-offs. TPE requires high spatiotemporal photon density, typically achieved using femtosecond laser sources with 100–150 fs pulse durations, 780–920 nm wavelengths, and high numerical aperture illumination [38–41]. In contrast, LSM requires low-NA illumination to generate a thin light sheet with an extended Rayleigh range. As a result, TP-LSM often produces weaker fluorescence signals, leading to reduced image quality. Approaches such as time-averaging methods [42,43], postprocessing techniques, and increasing average power have been explored to compensate, but these methods are either incompatible with real-time imaging or pose an increased risk of phototoxicity due to higher average power. Thus, there remains a critical need to enhance TP-LSM image quality without increasing average power or extending acquisition time.

Recently, several studies have explored strategies to improve fluorescence generation efficiency by exploiting the quadratic dependence of TPE on pulse energy. Because TPE relies on pulsed laser sources, the fluorescence yield depends not only on the average power but also on how the excitation energy is distributed among individual pulses. By redistributing the same average power into fewer, higher-energy pulses, it is possible to enhance fluorescence generation efficiency without increasing the total energy delivered to the sample. This property has motivated recent efforts to optimize pulse parameters such as repetition rate and pulse energy in multiphoton imaging systems [44–46]. However, in practical imaging systems, the usable average power delivered to the sample is often limited by optical transmission losses introduced by pulse-picking components and the available output power of femtosecond laser sources. Consequently, a practical trade-off exists among pulse energy, repetition rate, and usable average power in multiphoton imaging systems.

This study reports the integration and systematic evaluation of a single-objective two-photon oblique light sheet microscopy (TP-ob-LSM) system that incorporates a low-repetition-rate light source. The single-objective configuration enables simultaneous excitation and detection, thereby expanding compatibility with larger and more complex samples. By integrating a femtosecond laser with a pulse picker to reduce repetition rate, we increased pulse energy at constant average power, thereby enhancing fluorescence generation and improving image quality. Conventional femtosecond lasers for TPE typically operate at 76–80 MHz with limited average power to avoid thermal damage, which consequently results in low pulse energy and inefficient fluorescence generation due to the quadratic dependence of TPE. In contrast, reducing the repetition rate concentrates energy into fewer, higher-energy pulses at the same average power, substantially improving signal-to-noise ratio (SNR) [47].

Although low-repetition-rate excitation can substantially enhance fluorescence generation, the usable average power delivered to the sample is constrained by optical losses introduced by pulse picking. In this work, we therefore focus on system-level optimization of the low-repetition-rate TP-ob-LSM system—balancing repetition rate and on-sample average power—to achieve significantly higher-SNR 3D imaging than high-repetition-rate excitation at comparable average power. We demonstrate the advantages of this approach through quantitative SNR analysis under realistic imaging conditions and imaging experiments in biological samples. Furthermore, we validate the system by performing high-resolution, large-area, deep-tissue imaging of mouse brain samples using only 11 mW of on-sample power, establishing low-repetition-rate, single-objective TP-ob-LSM as a promising platform for high-quality 3D biomedical imaging.

2. METHOD

A. System Development

Figure 1(a) shows the schematic of the TP-ob-LSM system. A 920 nm femtosecond pulsed laser (ALCOR 920-2, Spark Lasers, France) was used to excite green fluorescent protein (GFP) in mouse brain tissue samples. To generate a tunable repetition-rate light source, a pulse picker (pulseSelect, APE, Germany) was integrated with the laser. The pulse picker, synchronized with the laser trigger, provided a low-repetition-rate output by integer division of the native 80 MHz pulse train. The laser beam emerging from the pulse picker was scanned by a galvanometer mirror (G1, GVS001, Thorlabs, Newton, New Jersey, USA) to form a virtual light sheet. The beam size was adjusted using a scan lens (S0, A254-200-AB-ML, Thorlabs, USA) and a tube lens (T0, AC254-100-AB-ML, Thorlabs, USA). The adjusted beam was directed to a second galvanometer mirror (G2, QS20X-AG, Thorlabs, USA) with a 4 mm offset and then relayed through a scan lens (S1, VIS-NIR #49-390, Edmund Optics, USA) and a tube lens (T1, VIS-NIR #49-392, Edmund Optics, USA) before entering the primary objective (O1, XLUMPLFLN20XW, 20× magnification, water immersion, numerical aperture 1.0, Olympus, Japan) with an 8 mm offset. The incident beam, 1.2 mm in diameter, formed an oblique light sheet tilted at 42° in the sample space, as shown in Fig. 1(b). G1 controlled the light sheet width, while G2 translated the tilted light sheet along the x axis, enabling 3D fluorescence imaging without mechanical sample movement.

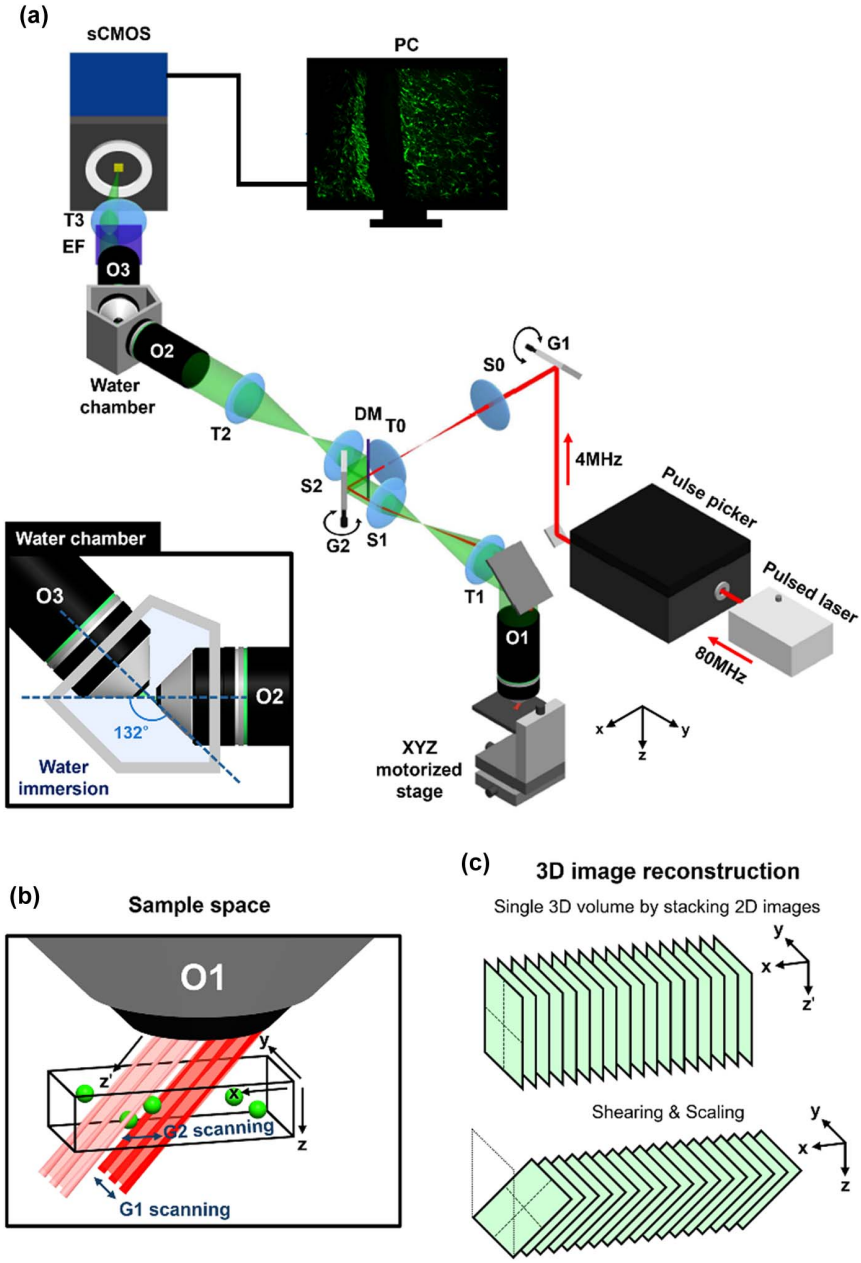

Fig. 1. Schematic of the two-photon oblique light sheet microscopy system. (a) Optical layout of the setup (O1–O3, objective lenses; T0–T3, tube lenses; S0–S2, scan lenses; DM, dichroic mirror; EF, emission filter; G1 and G2, galvanometer mirrors). (b) Oblique light sheet geometry showing illumination tilted at 42° in the sample space. (c) Image reconstruction process illustrating the transformation of acquired 2D oblique image stacks into distortion-corrected 3D volumes through affine shearing and scaling transformations.

The light sheet had a thickness of 4.86 μm and a Rayleigh range of 180 μm, resulting from a low effective NA associated with the small illumination beam diameter. The spatial resolution of the TP-ob-LSM system was estimated from the system point spread function (PSF), derived by multiplying the illumination and detection PSFs. Based on the full width at half maximum of the system PSF, the resolution was calculated as 0.73 μm × 0.36 μm laterally (x–y) and 1.10 μm axially (z).

Fluorescence signals generated in the y–z' image plane were descanned and reflected by a dichroic mirror (DM, FF735-Di02-25 × 36, Semrock, USA) and then relayed through a scan lens (S2, AC254-200-A-ML, Thorlabs, USA), a tube lens (T2, AC254-100-A-ML, Thorlabs, USA), and a second objective (O2, XLUMPLFLN20XW, Olympus, Japan) to form an optical refocusing system that produced a conjugate image. The magnification from O1 to O2 was designed to be unity, matching the refractive index ratio of the immersion media of both objectives and generating an aberration-free conjugate image [48]. This image was captured by an sCMOS rolling-shutter camera (pco.edge 4.2 bi, Excelitas, USA), which provides a 2048 × 2048-pixel sensor array with

an effective pixel size corresponding to 0.3 μm in the sample planes, ensuring high spatial sampling fidelity.

A detection assembly (O3-sCMOS) was positioned perpendicular to the image plane to deliver the conjugate image to the sCMOS camera. The image passed through an additional objective (O3, XLUMPLFLN20XW, Olympus, Japan) and a tube lens (T3, AC254-200-A-ML, Thorlabs, USA), providing 22× magnification before reaching the camera. An emission filter (EF, FF01-680/SP-25, Semrock, USA) suppressed background noise and selectively transmitted TPE-induced fluorescence. Further suppression of background noise was achieved by synchronizing the sCMOS rolling shutter with the illumination beam position, thereby implementing a confocal-slit effect.

To enhance fluorescence collection efficiency and maintain optical fidelity, a custom water chamber was implemented between objectives O2 and O3. In this configuration, high numerical aperture water-immersion objectives were used instead of low numerical aperture dry objectives, effectively increasing the collection efficiency of the detection path. The water chamber was designed to accommodate O2 and O3 in a 132° angular configuration, representing the orthogonal detection geometry (90°) relative to the image plane tilted by 42°. This allows O3 to be positioned perpendicular to the conjugate image plane while the space between the objectives is fully filled with water to prevent refractive index mismatch. Based on geometric optics calculations, the effective collection numerical aperture of the relay system was estimated to be approximately 0.56, corresponding to a fluorescence transmission efficiency of approximately 42%. Additionally, the chamber structure shields the optical space between the two objectives from external light during imaging, thereby reducing background noise.

The acquired 2D images were transferred to a computer and displayed in real time using custom software programmed in C++. Image stacks along the y–z' direction were reconstructed into a 3D volume, as illustrated in Fig. 1(c). Since simple stacking produces geometric distortion from the oblique plane geometry, affine transformations were applied, including scaling by 1/cos(42°) and a 42° shearing correction, to generate distortion-free 3D reconstructions.

B. Sample Preparation

1. Animals

All animal experiments were performed according to the protocols approved by KAIST IACUC, which follows the National Institutes of Health Guide for the Care and Use of Laboratory Animals. We used 14–17 weeks old male Thy1-GFP M transgenic mice (Jackson Laboratory, Cat. No. 007788).

2. Tissue Processing and Clearing

Briefly, we performed tissue fixation and clearing using the stabilization under harsh conditions via intramolecular epoxide linkage to prevent degradation (SHIELD) technique [49,50].

Perfusion We anesthetized the mice via intraperitoneal injection of 1.25% volume fraction avertin [44 mM (M, mol/L) 2,2,2-tribromoethyl alcohol (T48402, Sigma-Aldrich, USA) and 2.5% volume fraction tert-amyl alcohol (8.06193, Supelco, USA) in deionized water] solution at a dose of 30 μL/g. Then the mice were transcardially perfused using ice-cold 1× PBS (AM9625, Nalgene, USA) 40 mL for 8 min. Afterwards, the mice were perfused with 20 mL of SHIELD perfusion solution [20% volume fraction P3PE (GE-38, Huntsman Corporation, USA) and 4% volume fraction PFA (15714-S, Electron Microscopy Sciences, USA) in 1× PBS] for 4 min. The brains were then harvested and incubated in the SHIELD perfusion solution at 4°C for 48 h.

SHIELD processing Brain samples were then transferred to the SHIELD-OFF solution and incubated at 4°C for 96 h, with a solution change halfway through. After the incubation, samples were moved to 37°C preheated SHIELD-ON solution [50 mM sodium carbonate (S7795, Sigma-Aldrich, USA), 50 mM sodium bicarbonate (S5761, Sigma-Aldrich, USA), and 0.02% mass concentration sodium azide (S2002, Sigma-Aldrich, USA) in deionized water] and incubated at 37°C for 24 h. Finally, the samples were washed with 1× PBSN [1× PBS (18912014, Gibco, USA) with 0.02% mass concentration sodium azide (S2002, Sigma-Aldrich, USA)] for at least 24 h at room temperature.

Sectioning SHIELD-processed brains were sectioned into 500-μm-thick coronal slices or 1000-μm-thick horizontal slices using a vibratome (VT1000S, Leica Biosystems, Germany). For the 1000-μm-thick horizontal section, each slice was cut once more along the midline using a sterile razor blade.

Delipidation The sections were delipidated for overnight in the delipidation solution at 45°C, which is composed of 10 mM boric acid (B6768, Sigma-Aldrich, USA), 100 mM sodium sulfite (S0505, Sigma-Aldrich, USA), and 300 mM sodium dodecyl sulfate (75746, Sigma-Aldrich, USA) dissolved in deionized water titrated to pH 9 using 4 M sodium hydroxide (S5881, Sigma-Aldrich, USA) with filtration using 0.2 m PES vacuum filter (10040-440, VWR, USA). After the delipidation, the samples were incubated in 1% PBSTN [1× PBSN with 1% volume fraction Triton-X (T9284, Sigma-Aldrich, USA)] at 37°C for 2 h. After the incubation, the samples were washed with 1× PBSN at room temperature multiple times.

Optical clearing Delipidated, SHIELD fixed brains were then incubated in the optical clearing solution [OCS; 7.49 M 2,2'-thiodiethanol (88561, Sigma-Aldrich, USA), 10.55 M dimethyl sulfoxide (36840, Alfa-Aesar, USA), and 3.23 M iohexol (RY20200510, ROYAL PHARM, China) dissolved in deionized water with filtration using a 0.2 μm PES vacuum filter]. First, the samples were incubated in 0.5× OCS (OCS:1× PBSN = 1:1) at room temperature for 2 h with shaking. Next, the samples were incubated in degassed 1× OCS at room temperature overnight with shaking.

C. Repetition-Rate Control

We implemented a system capable of acquiring fluorescence signals with enhanced efficiency by employing a low-repetition-rate light source while maintaining the same average power. A pulse picker, integrated with the femtosecond laser, was used to control both the pulse repetition rate and the pulse energy. As shown in Fig. 2, the repetition rate was reduced from 80 to 4 MHz by selecting every 20th pulse from the original 80 MHz pulse train. With average power held constant, each pulse at 4 MHz carried 20-fold higher energy compared to the conventional 80 MHz system.

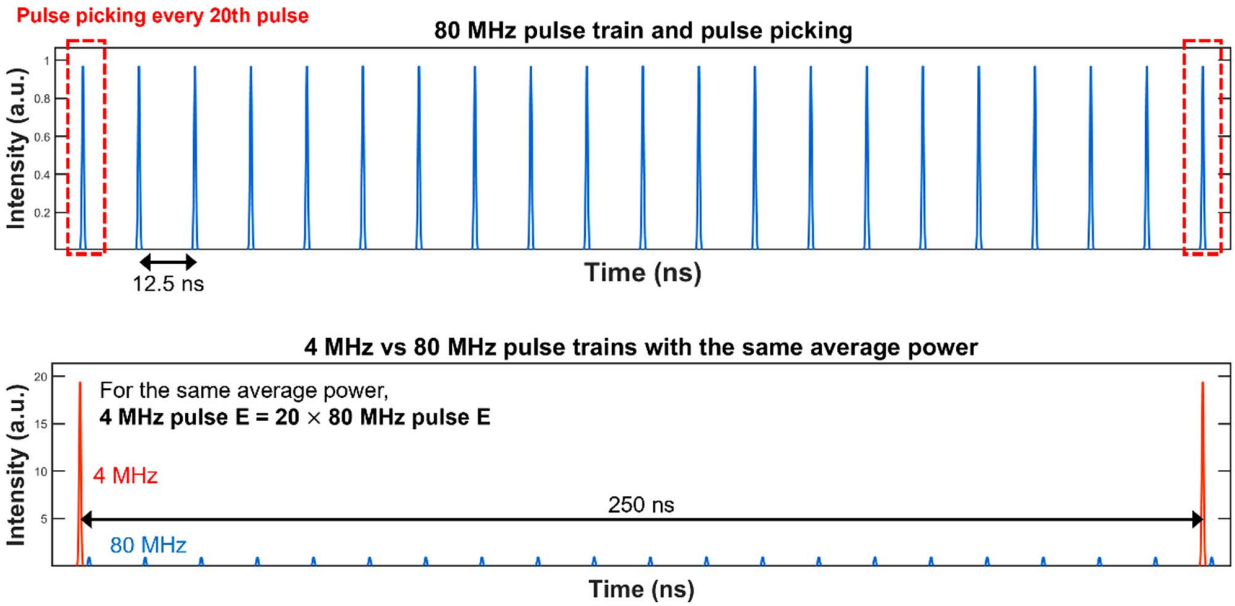

Fig. 2. Implementation of a low-repetition-rate light source using a pulse picker. The pulse picker selects every 20th pulse from the original 80 MHz femtosecond laser pulse train to generate a 4 MHz output. (Bottom) At 4 MHz, each pulse carries 20-fold higher energy than at 80 MHz at the same average power.

Such high pulse energy substantially increases fluorescence signal generation according to the quadratic dependence of TPE. The fluorescence signal per pulse is proportional to the square of the pulse energy. The number of photons absorbed per pulse, n, is expressed as follows [26]:

$$n \propto \frac{E_p^2}{\tau_p}\left(\frac{\mathrm{NA}^2}{2hc\lambda}\right)^2, \tag{1}$$

where E_p is the pulse energy, τ_p is the pulse duration, λ is the excitation wavelength, NA is the numerical aperture of the illumination, h is Planck's constant, and c is the speed of light. The total fluorescence signal per unit time is proportional to the product of signal per pulse and the pulse repetition rate. Therefore, reducing the repetition rate to 4 MHz was expected to increase the fluorescence signal by approximately 20-fold compared with the conventional 80 MHz system. This improvement directly translates to an estimated 20-fold enhancement in SNR under the same imaging conditions, except for the repetition rate, maintaining the same average power and imaging speed. The SNR, defined as the ratio of mean fluorescence intensity to the standard deviation of background noise, is given by [51,52]

$$\mathrm{SNR} = \frac{\overline{I_F}}{\sigma_{\mathrm{bg}}}, \tag{2}$$

where $\overline{I_F}$ is the mean fluorescence intensity, and σ_{bg} is the standard deviation of the background noise. To quantify the background noise term in Eq. (2), detector noise was measured under dark conditions using the same camera settings as those used during imaging. Background images were acquired while the excitation laser remained on but without the sample present in the optical path. The standard deviation of pixel intensities in these dark-condition images was used to estimate the detector background noise σ_{bg}. This procedure accounts for the dominant detector noise sources, including camera read noise and dark noise. Because the detector settings remained unchanged across all repetition-rate conditions, the background noise level was assumed to remain constant during the SNR comparison.

In this system, reducing the laser repetition rate increases the energy per pulse, which, under a fixed average power, theoretically enhances two-photon fluorescence efficiency and enables higher-SNR imaging within shorter acquisition times compared to high-repetition-rate excitation. In practice, however, the achievable excitation conditions are constrained by both the laser output characteristics and the diffraction efficiency of the pulse picker.

At repetition rates higher than 4 MHz, the diffraction efficiency of the acousto-optic modulator (AOM) decreases significantly, resulting in increased optical power loss and limiting the usable pulse energy delivered to the sample. For example, at 8 MHz the usable pulse energy is limited to approximately 1.75 nJ per pulse (14 mW/8 MHz) under our experimental conditions, and at higher repetition rates the usable pulse energy becomes further reduced due to increased optical losses in the pulse-picking process. Conversely, at repetition rates lower than 4 MHz, although the AOM efficiency improves, the reduced number of pulses restricts the usable average power to less than 5–6 mW, which is insufficient for stable high-SNR imaging. Under these constraints, we performed a system-level optimization to balance the requirements on repetition rate and on-sample average power. When the pulse picker was set to 4 MHz and the maximum permissible pulse energy from the laser was used, an average power of 11 mW could be reliably delivered to the sample, corresponding to a pulse energy of approximately 2.75 nJ per pulse (11 mW/4 MHz). Therefore, considering the trade-off between pulse energy and usable average power, we selected 4 MHz as the operating repetition rate for the TP-ob-LSM system.

3. RESULTS

A. Signal-to-Noise Ratio Analysis of 3D Mouse Brain Images

Using the TP-ob-LSM system, we acquired 3D two-photon fluorescence images of biological samples and evaluated the SNR at different repetition rates. We further compared image quality between a high-repetition-rate system employing a signal-averaging method and a low-repetition-rate light source.

Figure 3 presents maximum-intensity z projections of fluorescence images from coronal sections of Thy1-GFP M mouse brain tissue. Figures 3(a) and 3(b) show images acquired with high- (80 MHz) and low-repetition-rate (4 MHz) light sources, respectively, under identical average power. Figure 3(c) shows the result of averaging 20 high-repetition-rate images. Enlarged views of the red and blue square regions are also provided for comparison. To demonstrate how the improved SNR facilitates

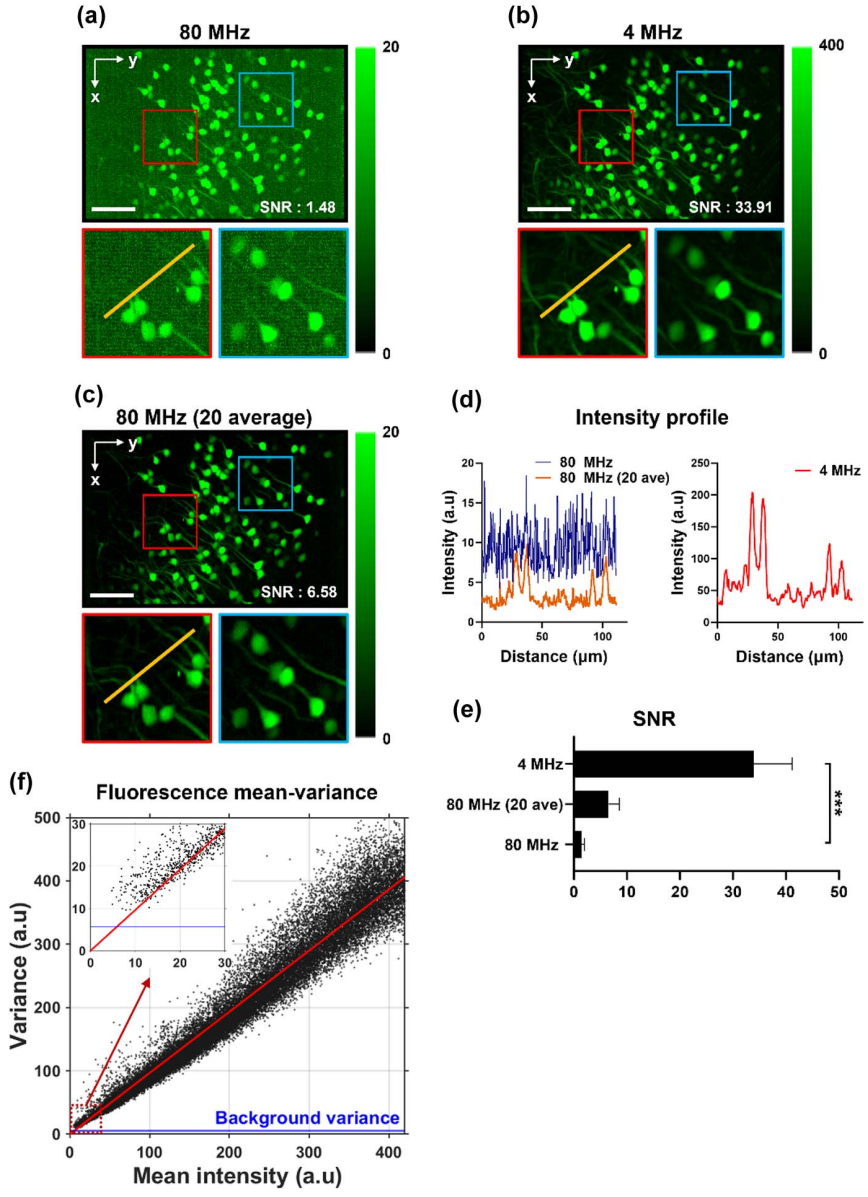

Fig. 3. Maximum-intensity z projections of coronal sections from Thy1-GFP M mouse brain tissue. (a) Single-scan image acquired at 80 MHz (SNR = 1.48 ± 0.49). (b) Single-scan image acquired at 4 MHz (SNR = 33.91 ± 7.26). (c) Averaged image obtained by accumulating 20 frames at 80 MHz (SNR = 6.58 ± 2.03). Insets show magnified views of the regions marked by the red and blue boxes. (d) Line-intensity profiles extracted along the yellow lines indicated in (a)–(c), comparing fluorescence signal across the dendritic structures under different imaging conditions (red, 4 MHz; blue, 80 MHz; orange, averaged 80 MHz). (e) Quantitative comparison of signal-to-noise ratio (SNR) across different imaging conditions. SNR values were calculated from 24 regions of interest (ROIs), with error bars indicating standard deviation. Statistical significance was evaluated using a two-tailed t-test (***$p < 0.001$). Scale bars: 100 μm. (f) Mean-variance plot constructed from repeated fluorescence imaging of the same location in a fluorescent slide, showing a linear increase in variance with fluorescence signal intensity, consistent with signal-dependent photon-noise behavior. The inset shows an enlarged view of the low-fluorescence-intensity region.

structural identification, line-intensity profiles were extracted along the yellow lines indicated in Figs. 3(a)–3(c), which cross representative dendritic structures. As shown in Fig. 3(d), the intensity profile obtained with 80 MHz excitation exhibits weak fluorescence signals relative to the surrounding background, making the dendritic structure difficult to distinguish. Frame averaging improves the visibility of the fluorescence signal; however, the signal contrast between dendritic structures and the background remains limited. In contrast, the 4 MHz excitation produces significantly higher signal contrast along the dendritic structures, clearly resolving the dendritic morphology and enabling more reliable identification of fine neuronal features. Previous studies report that dendrites of pyramidal neurons typically have diameters of approximately 2–3 μm and gradually increase toward the soma [53]. In our measurement, the extracted intensity profiles clearly delineate the dendritic structures along the indicated regions. Figure 3(e) summarizes a quantitative comparison of the mean SNR and standard deviation under each condition. To remove fixed-pattern noise inherent to the sCMOS camera, 400 dark images were averaged to generate a background noise map, which was then subtracted from the raw dataset prior to SNR calculation. The SNR was computed from 24 regions of interest (ROIs) containing multiple neuronal structures by dividing the mean fluorescence intensity in each ROI by the standard deviation of noise obtained from dark images. The calculated SNR values are indicated below each image. Statistical analysis was performed using a two-tailed t-test, demonstrating that the low-repetition-rate (4 MHz) excitation provides significantly higher SNR than the 80 MHz condition ($^{***}p < 0.001$). All images were acquired at a sample power of 11 mW and a frame rate of 20 fps, with each volume consisting of 400 frames acquired in 20 s. Images were processed using maximum-intensity z projections from volumetric data of 400 μm × 600 μm × 180 μm.

The measured SNR values were 1.48 for the high-repetition-rate image [Fig. 3(a)], 33.91 for the low-repetition-rate image [Fig. 3(b)], and 6.58 for the averaged high-repetition-rate image [Fig. 3(c)]. With the high-repetition-rate light source, relatively weak two-photon fluorescence signals were generated due to the reduced pulse energy. In contrast, the low-repetition-rate (4 MHz) light source achieved a 22.9-fold improvement in SNR under the same average power. In the magnified view of Fig. 3(b), thin and elongated dendritic structures were clearly observed. Because imaging conditions other than the repetition rate were identical, the background noise levels were expected to remain constant. To verify this assumption, the detector background noise was experimentally measured under dark conditions while maintaining identical detector settings. The measured background noise level was 1.69 digital number (DN). Based on the manufacturer specifications of the sCMOS camera, including a read noise of 1.0 e-, a dark current of 0.2 e-/(pixel·s), an exposure time of 733 μs, and a conversion gain of 0.7 e-/DN, the theoretical detector noise is estimated to be approximately 1.43 DN using the total effective noise equation [54]. The close agreement between the experimentally measured noise and the theoretically estimated detector noise indicates that the background noise is primarily dominated by detector-related noise sources. Thus, the improvement in SNR with the low-repetition-rate light source is primarily attributed to the increased fluorescence signal intensity. Because the background noise level remained nearly constant under identical detector settings, the 22.9-fold increase in SNR directly reflects a corresponding increase in the detected fluorescence signal. This experimentally observed enhancement is therefore in good agreement with the theoretical predictions of 20-fold increase in fluorescence signal, which arises from the quadratic dependence of two-photon excitation on pulse energy.

To further examine the noise behavior under fluorescence imaging conditions, we repeatedly acquired 400 fluorescence images from the same location in a fluorescent slide (FSK2, Thorlabs, USA) and evaluated the fluctuations of fluorescence signals at the individual-pixel level to construct a mean-variance plot [Fig. 3(f)]. The analysis showed that the variance increased approximately linearly with fluorescence signal intensity, indicating the presence of a signal-dependent photon-noise component. Within the signal range corresponding to the 4 MHz condition, the contribution of signal-dependent noise became more pronounced, whereas within the signal range corresponding to the 80 MHz condition, detector-related noise contributed more substantially.

For comparison between the averaging method and the low-repetition-rate source approach, SNR analysis was performed under conditions producing equivalent total fluorescence emission. Averaging 20 high-repetition-rate frames improved the SNR by 4.45-fold compared to a single frame, closely matching the theoretical improvement of $\sqrt{20} = 4.47$, confirming that the gain resulted primarily from statistical noise reduction rather than increased fluorescence generation. Notably, averaging 20 frames required 20 times longer acquisition time and 20 times greater illumination energy, yet the resulting SNR value remained significantly lower than that obtained with the low-repetition-rate source. Despite generating the equivalent overall fluorescence emission, the averaging approach yielded lower SNR than the low-repetition-rate excitation, revealing the superior two-photon excitation efficiency of high pulse energy illumination.

B. Large-Area High-Resolution Imaging with Single-Objective TP-ob-LSM System

To demonstrate the applicability of the single-objective TP-ob-LSM system for imaging samples of varying sizes and types, we performed large-area, high-resolution imaging of Thy1-GFP M mouse brain coronal sections using a low-repetition-rate (4 MHz) light source. Using a motorized stage, a total of 598 volumetric datasets were acquired through raster scanning with 30% overlap between adjacent volumes. Each volumetric dataset required 20 s for acquisition, resulting in a total imaging time of approximately 3.5 h for the entire dataset. These volumetric images were stitched in ImageJ to reconstruct the entire transverse brain slice. The reconstructed dataset captured fluorescence signals from neurons in the cerebral cortex, hippocampus, superior colliculus, reticular nuclei, and pons (Fig. 4).

Figure 4(a) shows a maximum intensity z projection of the reconstructed 3D volume spanning 9 mm × 6 mm × 0.18 mm. A magnified view of the red rectangular ROI in Fig. 4(a) is shown in Fig. 4(b), highlighting pyramidal neurons

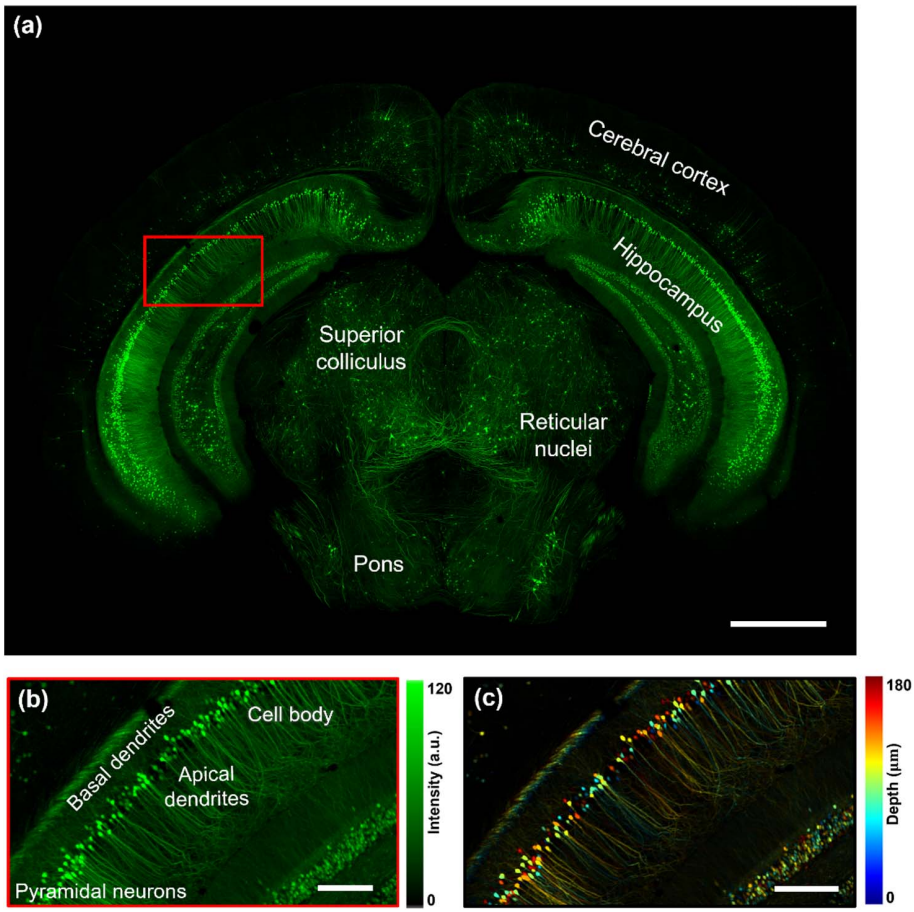

Fig. 4. Large-area high-resolution imaging of mouse brain tissue using the single-objective TP-ob-LSM with a 4 MHz light source. (a) Reconstructed large-area image of a Thy1-GFP M mouse brain coronal section (9 mm × 6 mm × 0.18 mm) obtained from 600 volumetric scans. (b) Magnified view of the red ROI region in (a), displaying pyramidal neurons with clearly resolved structures. (c) Depth-encoded intensity image of the same region, visualizing depth information across 180 μm. Scale bars: (a) 1 mm and (b), (c) 200 μm.

in the hippocampus with clearly resolved cell bodies and distinct apical and basal dendrites. Figure 4(c) presents a depth-encoded intensity image of the same ROI, with color indicating relative imaging depth (red, deeper layers; blue, superficial layers).

These results demonstrate that the single-objective TP-ob-LSM system enables efficient acquisition of high-resolution 3D images over large fields of view, providing detailed visualization of fine neural structures across diverse anatomical regions.

C. 3D Deep-Tissue Imaging Using TP-ob-LSM

We performed 3D volumetric imaging of thick biological tissues using the TP-ob-LSM system. The system employed a sample-objective lens with a 1 mm working distance, enabling imaging of tissue samples up to 1 mm in thickness. Figure 5 presents 3D imaging results from the hippocampus region of Thy1-GFP M mouse brain slices. Depth imaging was carried out in 11 steps along the z axis using a motorized stage with 50% overlap, and the resulting volumetric datasets were stitched in ImageJ. In total, 99 volumetric datasets were acquired, resulting in a total acquisition time of approximately 30 min.

Figures 5(a)–5(c) display maximum intensity projections along the x–z, x–y, and y–z planes, respectively, while Fig. 5(d) presents a 3D rendering generated with Imaris software. The reconstructed volume measured approximately 900 μm × 1400 μm × 800 μm, indicating that the original 1-mm-thick tissue sample had undergone optical clearing and contracted to approximately 800 μm. The rendering reveals fluorescent neuronal structures extending continuously along the depth axis, demonstrating that the TP-ob-LSM system provides high-quality 3D imaging deep within biological tissues.

4. DISCUSSION

In this study, we developed a single-objective TP-ob-LSM system utilizing a low-repetition-rate femtosecond laser for high-efficiency, high-resolution 3D fluorescence imaging. By combining TPE with an oblique light sheet geometry in a single-objective configuration, the proposed system addresses several key limitations of conventional TP-LSM approaches. These include restricted sample compatibility, weak fluorescence signals under high-repetition-rate and low-NA excitation, and photo-thermal damage caused by elevated average power. The single-objective design enables simultaneous fluorescence excitation and detection, significantly improving accessibility to

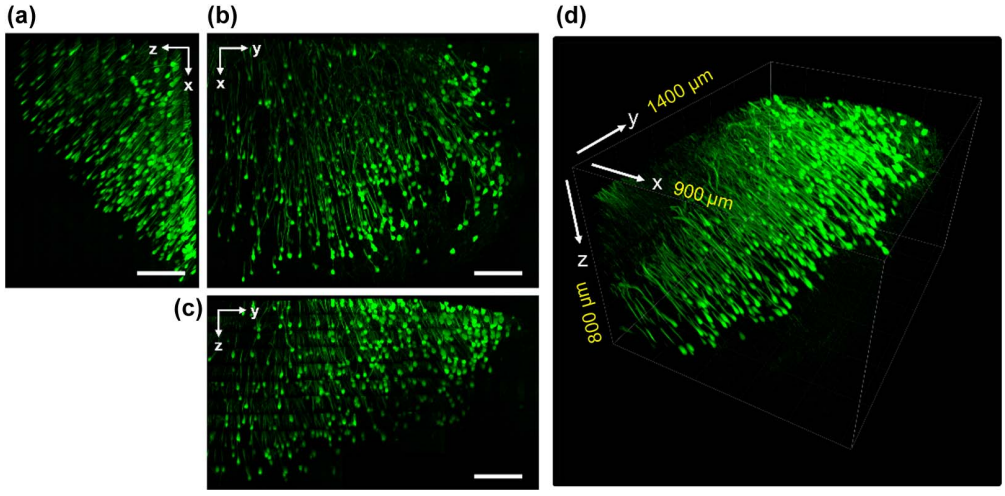

Fig. 5. 3D deep-tissue imaging of mouse hippocampus using TP-ob-LSM. (a)–(c) Maximum-intensity projection of Thy1-GFP M mouse brain tissue along the *y*, *z*, and *x* axes, respectively, acquired through 11-step depth imaging. (d) 3D volumetric rendering generated with Imaris software. Scale bars: 200 μm.

diverse biological samples while offering a low thermal damage approach for deep-tissue 3D imaging.

A central contribution of this work is the systematic integration of tunable low-repetition-rate excitation within a single-objective TP-ob-LSM system. This is achieved by integrating a pulse picker with a femtosecond laser, allowing the repetition rate to be reduced from 80 to 4 MHz while maintaining constant average power on the sample. Under these conditions, the energy per pulse increases by 20-fold. Given the quadratic dependence of two-photon fluorescence generation on pulse energy, this approach significantly enhances fluorescence signal strength without increasing the risk of thermal damage. Consequently, it is expected to yield a 20-fold improvement in SNR compared to conventional high-repetition-rate excitation. At the same time, the pulse-picking process introduces optical losses that limit the maximum usable pulse energy delivered to the sample. We therefore performed a system-level optimization of the low-repetition-rate TP-ob-LSM system.

We validated the performance of TP-ob-LSM by imaging Thy1-GFP M mouse brain sections at both high (80 MHz) and low (4 MHz) repetition rates, keeping all other imaging parameters constant. While images acquired at 80 MHz showed weak fluorescence signals (SNR = 1.48), those at 4 MHz achieved a 22.9-fold higher SNR, closely matching the theoretical predictions. Notably, even when averaging 20 high-repetition-rate frames to match the total fluorescence emission, the resulting SNR remained significantly lower than that of the single frame acquired with the low repetition rate. This confirms that frame averaging cannot compensate for the inherently lower fluorescence signal generated by high-repetition-rate excitation. These results clearly demonstrate that optimized low-repetition-rate excitation achieves substantially higher fluorescence signal and improved SNR within shorter acquisition times, while maintaining the same on-sample average power.

Beyond SNR enhancement, the single-objective configuration of the TP-ob-LSM system allows improved flexibility in sample size and geometry, expanding its applicability to larger or intact biological specimens. We demonstrated large-area imaging by stitching 600 volumetric datasets covering a 9 mm × 6 mm × 0.18 mm brain tissue section, revealing subcellular structures such as apical and basal dendrites across multiple anatomical regions. Furthermore, we performed deep-tissue imaging on 1-mm-thick cleared brain slices, successfully visualizing extended neuronal projections and confirming the system's capability for deep high-resolution 3D volumetric imaging in thick tissue.

Despite these strengths, several challenges remain. First, the pulse picker introduces optical losses that limit the maximum usable power delivered to the sample. The achievable pulse energy is fundamentally constrained by the available output power of the femtosecond laser source. As the repetition rate decreases, maintaining sufficient average power at the sample becomes increasingly challenging due to these optical losses and laser power limitations. Nevertheless, in our study, an on-sample power of only 11 mW, which is lower than that typically used in two-photon microscopy [55–57], was sufficient to obtain high-SNR images due to the improved excitation efficiency at low repetition rate. Additionally, large-area or deep-tissue imaging still requires extended acquisition times due to mechanical stage movement and camera frame rate limitations. Future work may explore the use of propagation-invariant beams, such as Bessel beams, to expand the field of view and reduce scanning demands. Moreover, while low-repetition-rate excitation enhances TPE efficiency without increasing average power, the elevated pulse energy may raise concerns about potential nonlinear phototoxicity. Although no visible photobleaching or photodamage was observed during repeated imaging in this study, the relationship between pulse energy and potential nonlinear photodamage remains an important consideration for practical applications. To ensure safe application *in vivo* or *in vitro* experiments, cell viability assays or potential damage indicators, such as abrupt fluorescence spikes, morphological changes, rapid fluorescence decay, or oxidative stress, should be carefully evaluated.

In conclusion, the low-repetition-rate-based, single-objective TP-ob-LSM system presented here demonstrates the effectiveness of integrating tunable repetition-rate control into an oblique light sheet system through system-level optimization. The single-objective configuration improves sample accessibility, while low-repetition-rate excitation significantly enhances fluorescence generation efficiency without increasing average power. Together, this systematic implementation and quantitative validation establish TP-ob-LSM as a powerful and versatile imaging platform for a wide range of biomedical applications, including high-throughput volumetric imaging in neuroscience, tissue engineering, and disease diagnostics.

Funding. National Research Foundation of Korea (RS-2026-25470369, RS-2025-25464869).

Disclosures. The authors declare no conflicts of interest.

Data Availability. Data underlying the results presented in this paper are not publicly available at this time but may be obtained from the authors upon reasonable request.

REFERENCES

1. A. D. Elliott, "Confocal microscopy: principles and modern practices," Curr. Protoc. Cytometry **92**, e68 (2020).
2. J. H. Strickler and W. W. Webb, "Two-photon excitation in laser scanning fluorescence microscopy," Proc. SPIE **1398**, 107–118 (1991).
3. C. L. Phillips, L. J. Arend, A. J. Filson, *et al.*, "Three-dimensional imaging of embryonic mouse kidney by two-photon microscopy," Am. J. Pathol. **158**, 49–55 (2001).
4. E. P. Perillo, J. E. McCracken, D. C. Fernée, *et al.*, "Deep *in vivo* two-photon microscopy with a low cost custom built mode-locked 1060 nm fiber laser," Biomed. Opt. Express **7**, 324–334 (2016).
5. M. He, D. Li, Z. Zheng, *et al.*, "Ultra-deep through-skull mouse brain imaging via the combination of skull optical clearing and three-photon microscopy," bioRxiv, 2021.12.20.473469 (2021).
6. H. Chen, H. Wang, M. N. Slipchenko, *et al.*, "A multimodal platform for nonlinear optical microscopy and microspectroscopy," Opt. Express **17**, 1282–1290 (2009).
7. M. Oheim, D. J. Michael, M. Geisbauer, *et al.*, "Principles of two-photon excitation fluorescence microscopy and other nonlinear imaging approaches," Adv. Drug Deliv. Rev. **58**, 788–808 (2006).
8. O. E. Olarte, J. Andilla, E. J. Gualda, *et al.*, "Light-sheet microscopy: a tutorial," Adv. Opt. Photonics **10**, 111–179 (2018).
9. J. Huisken and D. Y. Stainier, "Selective plane illumination microscopy techniques in developmental biology," Development **136**, 1963–1975 (2009).
10. J. Huisken, J. Swoger, S. Lindek, *et al.*, "Selective plane illumination microscopy," in *Handbook of Biological Confocal Microscopy* (Springer, 2006), pp. 672–679.
11. D. Kromm, T. Thumberger, and J. Wittbrodt, "An eye on light-sheet microscopy," in *Methods in Cell Biology* (Elsevier, 2016), pp. 105–123.
12. K. Khairy, W. C. Lemon, F. Amat, *et al.*, "Light sheet-based imaging and analysis of early embryogenesis in the fruit fly," in *Tissue Morphogenesis: Methods and Protocols* (Springer, 2014), pp. 79–97.
13. M. Weber and J. Huisken, "*In vivo* imaging of cardiac development and function in zebrafish using light sheet microscopy," Swiss Med. Wkly. **145**, w14227 (2015).
14. P. Fei, J. Lee, R. R. S. Packard, *et al.*, "Cardiac light-sheet fluorescent microscopy for multi-scale and rapid imaging of architecture and function," Sci. Rep. **6**, 22489 (2016).
15. T. Mano, A. Albanese, H.-U. Dodt, *et al.*, "Whole-brain analysis of cells and circuits by tissue clearing and light-sheet microscopy," J. Neurosci. **38**, 9330–9337 (2018).
16. M. Almasian, A. Saberigarakani, X. Zhang, *et al.*, "Light-sheet imaging to reveal cardiac structure in rodent hearts," J. Vis. Exp. **205**, e66707 (2024).
17. M. Weber, M. Mickoleit, and J. Huisken, "Multilayer mounting for long-term light sheet microscopy of zebrafish," J. Vis. Exp. **84**, e51119 (2014).
18. M. B. Meddens, S. Liu, P. S. Finnegan, *et al.*, "Single objective light-sheet microscopy for high-speed whole-cell 3D super-resolution," Biomed. Opt. Express **7**, 2219–2236 (2016).
19. S. An, K. F. Ziegler, P. Zhang, *et al.*, "Axial plane single-molecule super-resolution microscopy of whole cells," Biomed. Opt. Express **11**, 461–479 (2019).
20. T. Li, S. Ota, J. Kim, *et al.*, "Axial plane optical microscopy," Sci. Rep. **4**, 7253 (2014).
21. S. Yordanov, K. Neuhaus, R. Hartmann, *et al.*, "Single-objective high-resolution confocal light sheet fluorescence microscopy for standard biological sample geometries," Biomed. Opt. Express **12**, 3372–3391 (2021).
22. C. Dunsby, "Optically sectioned imaging by oblique plane microscopy," Opt. Express **16**, 20306–20316 (2008).
23. M. B. Bouchard, V. Voleti, C. S. Mendes, *et al.*, "Swept confocally-aligned planar excitation (SCAPE) microscopy for high-speed volumetric imaging of behaving organisms," Nat. Photonics **9**, 113–119 (2015).
24. V. Voleti, K. B. Patel, W. Li, *et al.*, "Real-time volumetric microscopy of *in vivo* dynamics and large-scale samples with SCAPE 2.0," Nat. Methods **16**, 1054–1062 (2019).
25. W. R. Zipfel, R. M. Williams, and W. W. Webb, "Nonlinear magic: multiphoton microscopy in the biosciences," Nat. Biotechnol. **21**, 1369–1377 (2003).
26. W. Denk, J. H. Strickler, and W. W. Webb, "Two-photon laser scanning fluorescence microscopy," Science **248**, 73–76 (1990).
27. F. Helmchen and W. Denk, "Deep tissue two-photon microscopy," Nat. Methods **2**, 932–940 (2005).
28. A. Diaspro, G. Chirico, and M. Collini, "Two-photon fluorescence excitation and related techniques in biological microscopy," Q. Rev. Biophys. **38**, 97–166 (2005).
29. Y. Dancik, A. Favre, C. J. Loy, *et al.*, "Use of multiphoton tomography and fluorescence lifetime imaging to investigate skin pigmentation *in vivo*," J. Biomed. Opt. **18**, 026022 (2013).
30. R. Cao, H. Wallrabe, and A. Periasamy, "Multiphoton FLIM imaging of NAD(P)H and FAD with one excitation wavelength," J. Biomed. Opt. **25**, 014510 (2020).
31. J. Li, X. Wu, Y. Fu, *et al.*, "Two-photon microscopy: application advantages and latest progress for *in vivo* imaging of neurons and blood vessels after ischemic stroke," Rev. Neurosci. **34**, 559–572 (2023).
32. H.-W. Wang, T. T. Le, and J.-X. Cheng, "Label-free imaging of arterial cells and extracellular matrix using a multimodal CARS microscope," Opt. Commun. **281**, 1813–1822 (2008).
33. J. Kang, U. Kang, H. S. Nam, *et al.*, "Label-free multimodal microscopy using a single light source and detector for biological imaging," Opt. Lett. **46**, 892–895 (2021).
34. S. G. Stanciu, S. Xu, Q. Peng, *et al.*, "Experimenting liver fibrosis diagnostic by two photon excitation microscopy and bag-of-features image classification," Sci. Rep. **4**, 4636 (2014).
35. P. Mahou, J. Vermot, E. Beaurepaire, *et al.*, "Multicolor two-photon light-sheet microscopy," Nat. Methods **11**, 600–601 (2014).
36. G. de Vito, L. Turrini, C. Fornetto, *et al.*, "Two-photon light-sheet microscopy for high-speed whole-brain functional imaging of zebrafish neuronal physiology and pathology," Proc. SPIE **11360**, 1136004 (2020).
37. S. Wolf, W. Supatto, G. Debrégeas, *et al.*, "Whole-brain functional imaging with two-photon light-sheet microscopy," Nat. Methods **12**, 379–380 (2015).
38. S. R. Kantelhardt, D. Kalasauskas, K. König, *et al.*, "*In vivo* multiphoton tomography and fluorescence lifetime imaging of human brain tumor tissue," J. Neuro-Oncology **127**, 473–482 (2016).
39. K. König, K. Schenke-Layland, I. Riemann, *et al.*, "Multiphoton autofluorescence imaging of intratissue elastic fibers," Biomaterials **26**, 495–500 (2005).

40. M. Oheim, E. Beaurepaire, E. Chaigneau, *et al.*, "Two-photon microscopy in brain tissue: parameters influencing the imaging depth," J. Neurosci. Methods **111**, 29–37 (2001).
41. M. van Zandvoort, W. Engels, K. Douma, *et al.*, "Two-photon microscopy for imaging of the (atherosclerotic) vascular wall: a proof of concept study," J. Vasc. Res. **41**, 54–63 (2004).
42. U. Hassan and M. S. Anwar, "Reducing noise by repetition: introduction to signal averaging," Eur. J. Phys. **31**, 453–465 (2010).
43. W. Tompkins, *Signal Averaging in Biomedical Digital Signal Processing* (Prentice Hall Englewood Cliffs, 1993).
44. M. J. Redlich, B. Prall, E. Canto-Said, *et al.*, "High-pulse-energy multiphoton imaging of neurons and oligodendrocytes in deep murine brain with a fiber laser," Sci. Rep. **11**, 7950 (2021).
45. L. Maddalena, M. Ouwehand, H. Safdar, *et al.*, "Flexible control of pulse intensity and repetition rate for multiphoton photostimulation," Front. Phys. **10**, 1005094 (2022).
46. K. Charan, B. Li, M. Wang, *et al.*, "Fiber-based tunable repetition rate source for deep tissue two-photon fluorescence microscopy," Biomed. Opt. Express **9**, 2304–2311 (2018).
47. J. Song, J. Kang, U. Kang, *et al.*, "SNR enhanced high-speed two-photon microscopy using a pulse picker and time gating detection," Sci. Rep. **13**, 14244 (2023).
48. E. J. Botcherby, R. Juškaitis, M. J. Booth, *et al.*, "An optical technique for remote focusing in microscopy," Opt. Commun. **281**, 880–887 (2008).
49. Y.-G. Park, C. H. Sohn, R. Chen, *et al.*, "Protection of tissue physicochemical properties using polyfunctional crosslinkers," Nat. Biotechnol. **37**, 73–83 (2019).
50. D. H. Yun, Y.-G. Park, J. H. Cho, *et al.*, "Uniform volumetric single-cell processing for organ-scale molecular phenotyping," Nat. Biotechnol. **43**, 2031–2042 (2025).
51. J. Cheon, Y. Chae, D. Kim, *et al.*, "Smart CMOS image sensor with high SBR and subpixel resolution for light-section-based range finding," IEEE Trans. Electron Dev. **56**, 2546–2555 (2009).
52. Z. He and J. Zhou, "Empirical evaluation of a new method for calculating signal-to-noise ratio for microarray data analysis," Appl. Environ. Microbiol. **74**, 2957–2966 (2008).
53. T. D. Helton, M. Zhao, S. Farris, *et al.*, "Diversity of dendritic morphology and entorhinal cortex synaptic effectiveness in mouse CA2 pyramidal neurons," Hippocampus **29**, 78–92 (2019).
54. G. C. Holst and T. S. Lomheim, *CMOS/CCD Sensors* (JCD Publishing, 2007).
55. C. Stosiek, O. Garaschuk, K. Holthoff, *et al.*, "*In vivo* two-photon calcium imaging of neuronal networks," Proc. Natl. Acad. Sci. U.S.A. **100**, 7319–7324 (2003).
56. Y. Bando, M. Wenzel, and R. Yuste, "Simultaneous two-photon imaging of action potentials and subthreshold inputs *in vivo*," Nat. Commun. **12**, 7229 (2021).
57. S. Han, W. Yang, and R. Yuste, "Two-color volumetric imaging of neuronal activity of cortical columns," Cell Rep. **27**, 2229–2240.e4 (2019).